Dynamic compression of copper to over 450 GPa: A high-pressure standard

R. G. Kraus,[1] J.-P. Davis,[2] C. T. Seagle,[2] D. E. Fratanduono,[1] D. C. Swift,[1] J. L. Brown,[2] and J. H. Eggert[1]
[1]*Lawrence Livermore National Laboratory, Livermore, California 94550, USA*
[2]*Sandia National Laboratories, Albuquerque, New Mexico 87185-1195, USA*
(Received 15 November 2015; revised manuscript received 1 March 2016; published 12 April 2016)

An absolute stress-density path for shocklessly compressed copper is obtained to over 450 GPa. A magnetic pressure drive is temporally tailored to generate shockless compression waves through over 2.5-mm-thick copper samples. The free-surface velocity data is analyzed for Lagrangian sound velocity using the iterative Lagrangian analysis (ILA) technique, which relies upon the method of characteristics. We correct for the effects of strength and plastic work heating to determine an isentropic compression path. By assuming a Debye model for the heat capacity, we can further correct the isentrope to an isotherm. Our determination of the isentrope and isotherm of copper represents a highly accurate pressure standard for copper to over 450 GPa.

DOI: 10.1103/PhysRevB.93.134105

I. INTRODUCTION

The high-pressure and low-temperature equation of state is critical to a number of natural science and engineering studies. For example, the equation of state of hydrogen is the dominant source of uncertainty in our understanding of the structure and composition of Jupiter's core [1], which has significant implications for our understanding of the formation of planets in our solar system. The abundance of extrasolar planets in the 1–10 Earth mass range is generating significant interest in the high-pressure properties of planetary minerals due to their effect on the structure and thermal evolution of super Earths and correspondingly potential planetary habitability. Central to these low-temperature high-pressure studies is the existence of a standard method of determining the stress state being studied. Attempts to develop accurate isothermal absolute-pressure standards using Brillouin scattering and x-ray diffraction have been limited to below 60 GPa [2], and therefore at higher pressures shock Hugoniot data are often used to constrain the low temperature isotherm due to the exact nature of the Rankine-Hugoniot relations, e.g., Refs. [3,4]. However, these shock-wave reduced isotherms (SWRI) require significant corrections from the measured Hugoniot states as the shock pressure and shock heating increases. Furthermore, the models for the thermal pressure are oftentimes not constrained by experimental data but determined from theoretical calculations, inhibiting rigorous error propagation. With the advancement of single stage diamond anvil cells reaching pressures of 375 GPa [5] and the advent of two-stage diamond anvil cells capable of reaching pressures greater than 770 GPa [6,7], there is a tremendous need for accurate pressure calibrants and rigorous error analysis in the range accessible to this novel diamond anvil cell technology.

Copper is commonly used as a pressure standard within the high-pressure community due to the availability of accurate shock wave data [3,4,8,9]. However, as discussed in Ref. [4], the shock wave reduced isotherm for copper is only valid to 200 GPa. The high-pressure behavior of copper is also critical to the capabilities at the Sandia Z machine [10], where copper is used as an electrode material in shockless compression experiments and as a flyer plate for ultrahigh velocity plate impact experiments [11]. Copper is also starting to be utilized as an ablator material for shockless compression experiments at the National Ignition Facility e.g., Ref. [12], and validation or improvement of the available equation of state models is critical to the design of future experiments.

Shockless compression experiments have previously been used to determine the high-pressure and low-temperature response of aluminum [13], diamond [12,14], and tantalum [15,16]. In this paper, we determine the stress-density response of shocklessly compressed copper. Copper is an excellent material to study by shockless compression experiments as it is expected to have no high-pressure phase transitions and low shear strength.

Using the Z pulsed-power accelerator at Sandia National Laboratories [10], magnetically driven uniaxial compression waves were generated in copper samples that ranged in thickness from ~2.4 to 3 mm thick. The Z accelerator produces a temporally shaped current pulse, of up to 20 MA and 1200 ns in duration that flows along the inner surface of the copper electrodes, generating a time-varying magnetic field. The interaction of the magnetic field and the current flux produces a time varying force on the inner surface of the copper electrodes, see schematic diagram in Fig. 1. In the stripline geometry, the samples on opposing sides of the short circuit loop undergo identical loading conditions, making this an excellent platform for shockless compression experiments.

II. EXPERIMENTAL METHOD

Two separate experiments, each with four sample pairs, were performed on copper: experiments Z2689 and Z2791. The OFE-OK grade copper electrodes were 99.998% pure with an average grain size of 80 μm and a measured HRF hardness of 43. The electrodes were 43.5 × 11 × 8 mm and slightly tapered at the base. Rectangular copper steps were diamond milled into the solid electrode to generate samples of the desired thickness, between ~2.4 and 3 mm thick and 9.0 × 7.7 mm in lateral dimension. The thickness of each copper sample was measured to an accuracy of ~3 μm.

The multipoint quadrature velocity interferometer system for any reflector (VISAR) operated at 532 nm. Three separate VISAR sensitivities were used on each sample, with fringe sensitivities that ranged from 257 to 483 m s^{-1} $fringe^{-1}$. After correcting the absolute timing of each VISAR channel for the etalon delay, individual free-surface velocities were

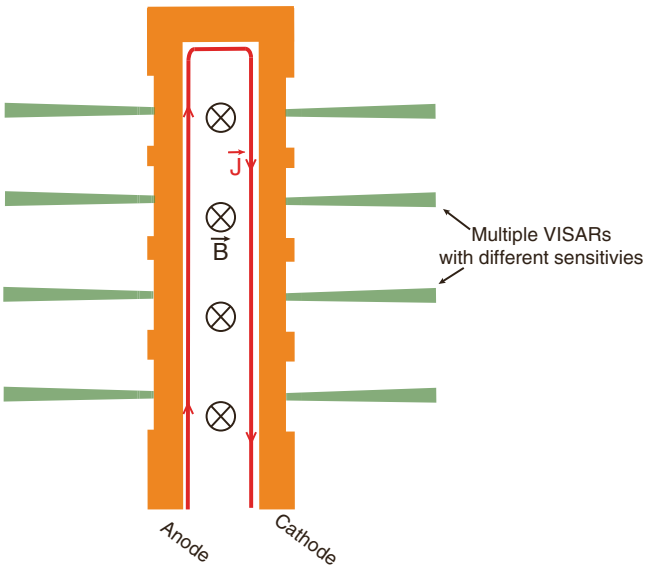

FIG. 1. Schematic stripline geometry used for the shockless compression experiment on copper. The current density (J) flows on the inner surface of the anode to the cathode, creating a magnetic field vector (B), which interacts with the current density and accelerates the anode and cathode away from each other. VISAR probes measure the free surface velocity of the copper anode and cathode and are shown in green.

averaged to reduce random uncertainties in the timing of individual VISAR channels, ∼0.2 ns, and the random phase uncertainty in the fringe count, ∼5% of the fringe sensitivity. Two-dimensional magnetohydrodynamic (MHD) simulations were performed to confirm that the 200 μm bare optical VISAR fibers were probing regions only undergoing uniaxial strain.

The averaged free-surface velocities from each sample pair for experiment Z2689 and Z2791 are presented in Figs. 2 and 3, respectively. One can see that in shot Z2689, Fig. 2, shockless compression data were obtained on all of the pairs up to a free-surface velocity of ∼3.5 km s^{-1}. In shot Z2791, Fig. 3, the current pulse shape was modified in order to avoid a shock forming in the middle of the pulse shape and shockless compression data were obtained on two of the pairs, N01-S01 and N02-S02, up to the peak free-surface velocity.

Due to the high electrical conductivity of copper, diffusion of the magnetic field through the copper samples is relatively slow. However, on shot Z2791, the pair N01-S01 shows that the peak velocity on N01 increases beyond the peak velocity of S01. This deviation is caused by the reverberation of the free-surface release wave with the magnetic diffusion front, which limits the range of analyzable data [17].

III. RESULTS

A. Stress-density analysis during shockless compression experiments

In an ideal shockless compression experiment, one would measure the in-material particle velocity as a function of time at multiple positions within the compressed sample [18].

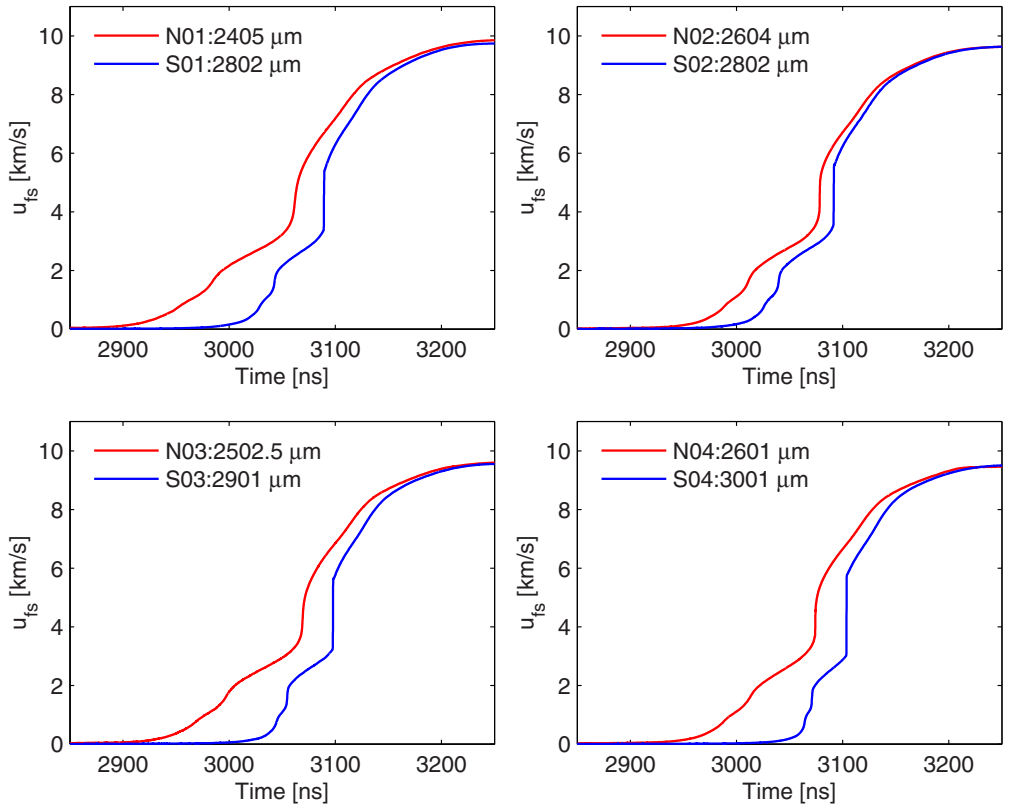

FIG. 2. Average free-surface velocity profiles for each of the four pairs of samples on shot Z2689. Shown within each subplot are the thickness measurements for both of the samples.

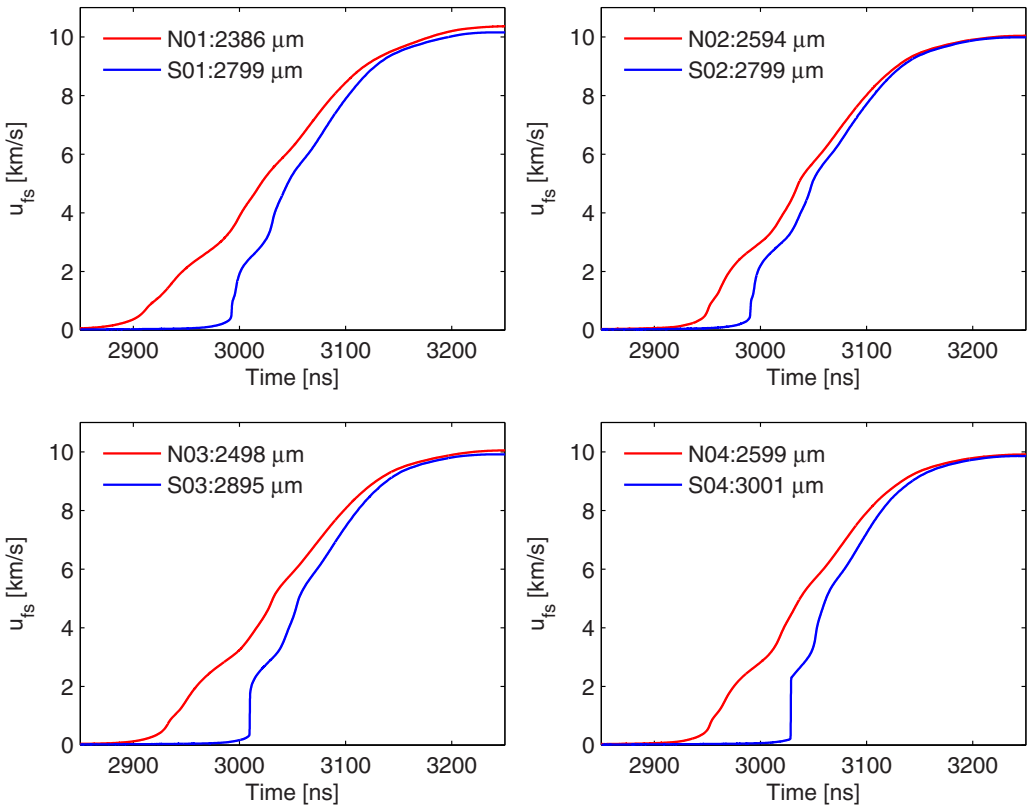

FIG. 3. Average free-surface velocity profiles for each of the four pairs of samples on shot Z2791. Shown within each subplot are the thickness measurements for both of the samples.

From the in-material particle velocity profiles, the Lagrangian sound speed is determined by the difference in measurement positions divided by the time it takes for a perturbation to travel from one position to the next, where a perturbation could be defined as an incremental increase in velocity. In this optimal shockless compression experiment, one could determine the Lagrangian sound speed C_L as a nearly continuous function of the in-material particle velocity u_p where $C_L = C_E \frac{\rho}{\rho_0}$ and C_E is the Eulerian sound velocity.

While in-material particle velocity profiles can be measured on insulators using techniques such as magnetic particle velocity gauges [19], for opaque metals one cannot measure a true in-material particle velocity and velocity profile measurements are limited to interfaces or free-surface velocity measurements. The iterative Lagrangian analysis (ILA) method [20,21] was developed to correct for the effect of the free surface reflection, or map the free-surface velocity profiles to in-material velocity profiles.

One way to consider the ILA method is that there is a unique solution to the isentropic equation of state for the problem where samples of two different thickness are shocklessly compressed by the same pressure boundary condition and the free surface velocity profiles are the problem constraints. The numerical techniques optimize over the equation of state and the pressure boundary condition until a solution matching the free surface velocity profiles is achieved. A more detailed description of the ILA method can be found in Ref. [15].

Recent work has shown that small shocks have a weak effect on the determination of the stress-density response using the ILA technique [22]; however, the data presented here are of sufficiently high accuracy to be sensitive to the small systematic error induced by analyzing data with small shocks. Therefore, only data without shocks are included in the analysis of the free-surface velocity measurements; this includes all the pairs from shot Z2689 up to 3.5 km s^{-1}. The data from Z2791 N01-S01 are included up to 8 km s^{-1} and Z2791 N02-S02 up to 8.8 km s^{-1}. The sound speeds and residuals from the weighted mean for each sample pair are presented as a function of free-surface velocity in Fig. 4.

The uncertainty in C_L is determined from the uncertainty in the slope of a fit to the Lagrangian thickness versus time for each particle velocity,

$$\left(\frac{\delta C_L}{C_L}\right)^2 = 2\left(\frac{\delta X}{X_2 - X_1}\right)^2 + 2\left(\frac{\delta t}{t_2 - t_1}\right)^2 + \left[\frac{\delta u_{p,1}}{(t_2 - t_1)du_{p,1}/dt}\right]^2 + \left[\frac{\delta u_{p,2}}{(t_2 - t_1)du_{p,2}/dt}\right]^2, \quad (1)$$

where $\delta X = 3$ μm is the measured thickness uncertainty for each step height X_2 and X_1, $\delta t = 0.12$ ns is the absolute timing uncertainty of the free-surface velocity profile, t_2 and t_1 are the in-material times where the steps reach the particle velocity of interest, $\delta u_{p,i} \approx 0.01$ km s^{-1} is the velocity uncertainty for profile i, and $du_{p,i}/dt$ is the acceleration at the time of interest. Consequently, the uncertainty in C_L is $\sim$1% for each sample pair. The weighted average Lagrangian sound velocity is determined as a function of free-surface velocity, weighted by $1/\delta C_L^2$. The uncertainty in this weighted average

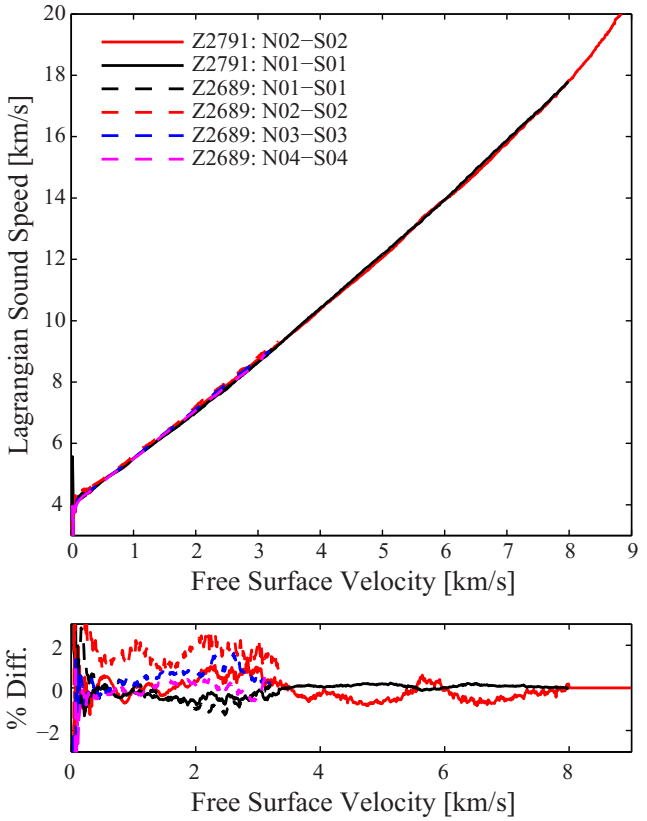

FIG. 4. Measured Lagrangian sound velocity as a function of the free-surface velocity for two pairs on shot Z2791 (solid lines) and 4 pairs on shot Z2689 (dashed lines). Below are plotted the residuals for each of the sound velocity measurements relative to the weighted average sound velocity of all the traces.

C_L is conservatively determined as the maximum of either the mean uncertainty in C_L, as determined by equation (1), or the standard deviation in C_L at each free-surface velocity.

The weighted average C_L can then be directly integrated to obtain the longitudinal stress σ_x and density ρ as a function of particle velocity u_p

$$\sigma_x = \rho_0 \int_0^{u_p} C_L du_p \tag{2}$$

and

$$\rho = \rho_0 \left[1 - \left(\int_0^{u_p} \frac{du_p}{C_L} \right) \right]^{-1}. \tag{3}$$

The uncertainties are propagated through the integrals to obtain uncertainties in longitudinal stress and density,

$$\delta\sigma_x = \rho_0 \int_0^{u_p} \delta C_L du_p, \tag{4}$$

and

$$\delta\rho = \frac{\rho^2}{\rho_0} \int_0^{u_p} \frac{\delta C_L du_p}{C_L^2}, \tag{5}$$

where the uncertainties are propagated linearly rather than in quadrature because the errors appear to be correlated rather than random.

A more complete description of the ILA technique can be found in Ref. [15]. Reference [15] also describes some of the issues facing the assumption of reversibility and isentropic flow inherent within the ILA technique, particularly for high-strength materials that exhibit significant time dependence. As copper is expected to have relatively low strength and to stay within the thermally activated regime over the stress range and strain rates considered in this study [23], the effects of rate dependence or irreversible flow should be negligible for copper. To test this assumption, we performed forward simulations of the ramp compression experiments using the ARES hydrocode [24]. These simulations utilized the SESAME 3325 equation of state for copper [25] and two different strength models: the standard time-independent Steinberg-Guinan strength model [26] and the Preston-Tonks-Wallace (PTW) strength model [23], which includes strain-rate dependence on the yield surface. We find that the ILA of simulated data generated with the PTW strength model disagrees with the simulated in-material stress density response by a small systematic difference of 0.3% in stress over the entire density range of interest, which is well below the experimental errors and thermomechanical corrections described here. The ILA of simulated data generated with the standard Steinberg-Guinan strength model is in nearly perfect agreement with the true in-material stress density response over the entire range of interest. Consequently, the ILA technique accurately determines the in-material stress-density response and any systematic contributions due to the ILA technique itself are small and can be ignored for copper.

B. Correcting shockless compression data for strength effects

Here we present a method for determining the principal isentrope and 298 K isotherm from the stress-density states that are determined from a shockless compression experiment. A correction is necessary because the stress-density path obtained by the ILA technique does not represent an isentrope due to strength and plastic work heating. For relatively low strength materials like copper, we find these corrections from the shockless compression data are small, ~2–3%, but because of the high accuracy of the experimental measurements, 2–4%, these corrections are now significant.

At this point forward we are considering an analysis of the thermodynamic states at constant density, consequently, the uncertainty in density is accounted for in the uncertainty in the stress state,

$$\delta\sigma_x(\rho)^2 = \delta\sigma_x(u_p)^2 + \left(\frac{\partial\sigma_x}{\partial\rho} \delta\rho(u_p) \right)^2. \tag{6}$$

Under uniaxial strain conditions, the longitudinal stress σ_x deviates from the mean hydrostatic stress P_{hyd} by an amount s_x, referred to as the stress deviator,

$$\sigma_x = P_{\text{hyd}} + s_x. \tag{7}$$

The work done by the stress deviators against plastic deformation of the material increases the entropy and temperature of the system. This source of dissipation is referred to as plastic work heating. For uniaxial strain conditions, and assuming a von Mises yield criterion [27], the differential amount of plastic work heating dW_p can be determined by the following

equation, derived in Ref. [28],

$$dW_p = \frac{1}{\rho_0}\frac{2}{3}Y[d\epsilon_x - (dY/2\mu)], \tag{8}$$

where Y is the yield strength, and μ is the shear modulus. For conditions of uniaxial strain, the natural strain ϵ_x is determined by the relative compression of the system according to

$$\epsilon_x = ln(\rho/\rho_0). \tag{9}$$

Assuming the material behaves quasiharmonically, the plastic work heating causes the mean hydrostatic pressure to deviate from an isentrope by

$$P_{\text{hyd}} - P_s = \gamma\rho \int_0^{\epsilon_x} \beta dW_p, \tag{10}$$

where γ is the Grüneisen parameter, P_s is the pressure on the principal isentrope, and β is the Taylor-Quinney factor, which describes the fraction of plastic work that partitions into thermal energy of the system [29]. Reference [29] found that for copper, $\beta = 0.9$. More recently, Ref. [30] found that for polycrystalline copper the Taylor-Quinney factor increases linearly with strain rate from 0.5 to 0.7 over a strain rate of 3000 to 8000 s^{-1}. The experiments considered here are at significantly higher strain rate, 10^6 s^{-1}, and a linear extrapolation of the results by Ref. [30] would suggest $\beta = 1$ at our high strain rates. In this paper, we assume a β of 0.9; however, because the strength of copper is low, the amount of plastic work is also small and the choice of β is relatively insensitive, as to decrease β by 50% only changes the final pressure on the isentrope by 0.3%.

Here we have made the simplifying assumption that only the fraction of plastic work that goes into thermal energy contributes to the pressure of the system. The other $(1 - \beta)$ of plastic work contributes to the potential energy of the lattice by creating defects, which in keeping with the assumption of deriving Eq. (8), is volume conserving.

1. Thermal pressure model

To determine the correction from the mean hydrostatic stress along the shockless compression path, P_{hyd} to the isentrope, P_s, we require a model for the Grüneisen parameter. The Grüneisen parameter is also useful for calculating the temperature change along an isentrope. Fortunately, the shockless compression data obtained here can be combined with porous Hugoniot data [31,32] and solid Hugoniot data [33–35] to constrain a Mie-Grüneisen equation of state for copper over the entire density range of interest. The Grüneisen parameter is determined at the density of each shock data point by the ratio of the difference in pressure to the difference in internal energy between the shock state, P_H and E_H, and the pressure and internal energy along an isentrope at the same density, P_S and E_S, respectively,

$$\gamma = \frac{(P_H - P_S)}{\rho(E_H - E_S)}, \tag{11}$$

where the internal energy on the Hugoniot is given by the Rankine-Hugoniot equations [36] and the internal energy along the isentrope is determined by integrating the first law of thermodynamics at constant entropy.

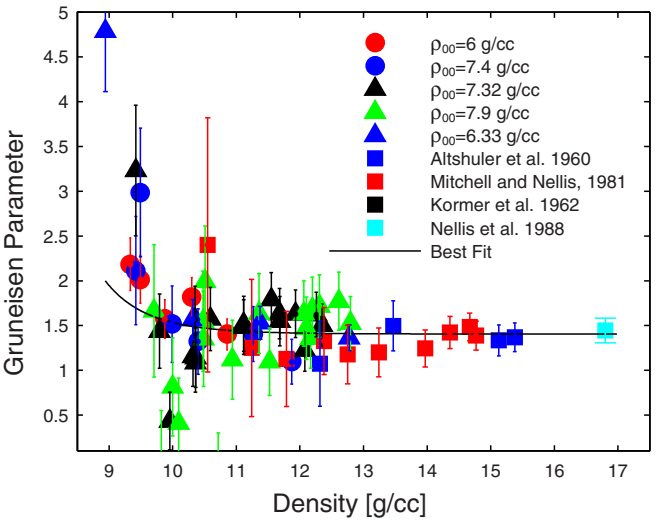

FIG. 5. Grüneisen parameter determined from comparison of principal and porous Hugoniot data with measured isentrope. Also included is our best fit.

The Grüneisen parameter data are fit to the Al'tshuler form of the density dependence of the Grüneisen parameter, which assumes the Grüneisen parameter is temperature independent,

$$\gamma = \gamma_\infty + (\gamma_0 - \gamma_\infty)\left(\frac{\rho_0}{\rho}\right)^\eta, \tag{12}$$

where γ_∞ is the infinite compression limit, η describes the density dependence, and γ_0 is the ambient pressure value, which we have fixed at the standard temperature and pressure value of 2.0(0.1) [37]. In Fig. 5, we present the Grüneisen parameters obtained using Eq. (11) for a range of initially porous and solid density Hugoniot data on copper. Also presented in Fig. 5 is our weighted nonlinear least squares fit to Eq. (12), where we find $\gamma_{inf} = 1.41$ and $\eta = 13.6$. As mentioned earlier, here we have made the assumption that the Grüneisen parameter is temperature independent. We find that this is a valid assumption based upon the agreement between the results of this technique and that of a local technique relating the sound speed along the Hugoniot to the slope of the Hugoniot, where Ref. [38] measured a γ of 1.55(15) at a density range of $\sim 14 - 15$ g cm^{-3} on the Hugoniot.

The standard deviation in the residuals and the average absolute residual between the experimental Grüneisen parameter and the best fit model are 0.68 and 0.38, respectively, which we believe to be overestimates of the uncertainty in the model as these metrics are dominated by a few data points with large scatter at low compressions. However, for the purposes of uncertainty propagation, we assume a ~25% uncertainty in the Grüneisen parameter, which propagates to a 0.2% uncertainty in the pressure on the isentrope. Unlike for shock-wave reduced isotherms, where the stress at high pressures becomes extremely sensitive to the thermal pressure model, here we find the pressure along the isentrope to be insensitive to the thermal model because of the relatively small amount of heating in the shockless compression experiment.

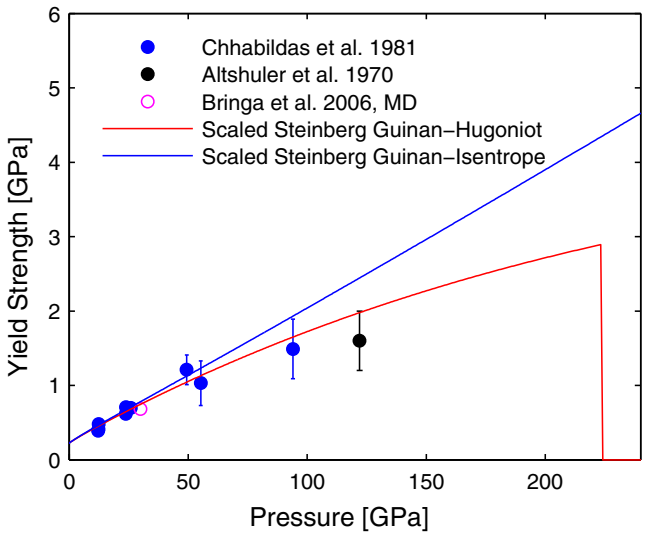

FIG. 6. High-pressure yield strength data determined along the principal Hugoniot. Also presented is a scaled fit to the Steinberg-Guinan strength model along the Hugoniot (red) and isentrope (blue), where the strength along the Hugoniot drops to zero at 224 GPa due to shock melting.

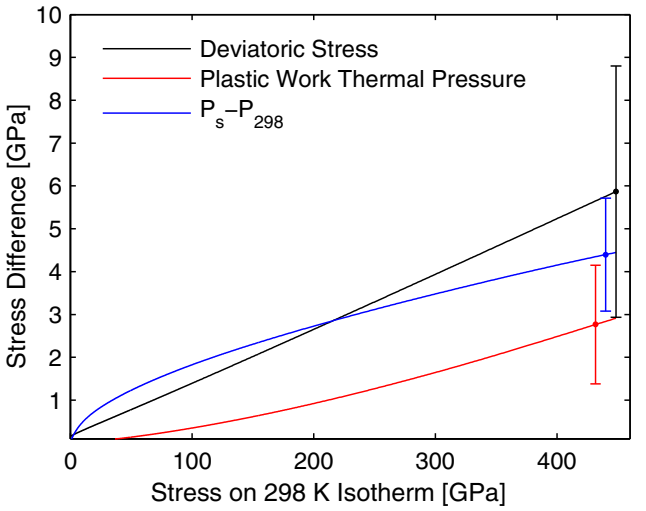

FIG. 7. Required corrections and associated uncertainties for reducing shockless compression data to the 298 K isotherm of copper. Plotted are the corrections for the deviatoric stress (black), thermal pressure due to plastic work heating (red), and thermal pressure correction from the principal isentrope to the 298 K isotherm (blue solid line).

2. *High pressure strength*

The high-pressure yield strength of copper has been measured on the shock Hugoniot by Refs. [39] and [40], and the data are presented in Fig. 6. The high-pressure yield strength of copper has also been calculated using molecular dynamics simulations by Ref. [41], which is in excellent agreement with the experimental data. We use a scaled Steinberg-Guinan model to fit the experimental yield strength of copper [26], where we scale the ambient pressure yield strength parameter, Y_0 and find the best fit to the yield strength data for $1.82Y_0$. In this case, the yield strength measurements on the copper Hugoniot achieve a similar strain rate to the shockless compression experiments. Consequently, we feel it is adequate to use a strain rate independent strength model, calibrated by gas gun data, to correct for the yield strength in the shockless compression experiments.

In order to correct for the yield strength over the entire range of pressures accessed by the shockless compression experiments, a significant extrapolation of the scaled Steinberg-Guinan is required. To account for this extrapolation in the correction at high pressures and at low temperatures along the shockless compression path, we assume a 50% uncertainty to the yield strength at high pressures. As copper is not expected to undergo a phase transition, and the experimental data and theoretical predictions are well represented by this empirical strength model, it is likely that we are overestimating the uncertainty in the yield strength. However, even such a large estimate in the uncertainty of the yield strength at high pressure only corresponds to an ∼1% uncertainty in the pressure on the isentrope. For comparison, the magnitude of the individual corrections from the shockless compression data to the 298 K isotherm are presented in Fig. 7.

3. *Hydrostatic Hugoniot states*

Although it is not often discussed in the literature, Hugoniot measurements should not be compared directly to equation of state models. One must correct Hugoniot data, at least within the solid phases, for the deviatoric stress and the thermal pressure generated due to plastic work heating. The plastic work heating along the Hugoniot can be calculated based upon the waste heat generated along the Rayleigh line by the longitudinal deviatoric stress, s_x [42],

$$W_{p,\mathrm{Hug}} = s_x\left(\frac{1}{\rho_0} - \frac{1}{\rho}\right). \tag{13}$$

The hydrostatic Hugoniot for a material is then given by

$$P_{\mathrm{Hug}} = \sigma_{x,\mathrm{Hug}} - s_x - \gamma\rho\beta W_{p,\mathrm{Hug}}, \tag{14}$$

where $\sigma_{x,\mathrm{Hug}}$ is the longitudinal stress at the Hugoniot state. For copper, this correction is equivalent to reducing the shock wave velocity in the solid by ∼0.025 km s^{-1} or ∼0.5%.

In order to correct all the porous Hugoniot and solid Hugoniot for strength effects, we must first determine the critical shock pressures for incipient melting of copper along the porous and solid density Hugoniots. We fit a Simon equation to the high-pressure melt curve of Ref. [43],

$$T_{\mathrm{melt}} = T_{\mathrm{Ref}}\left(\frac{P - P_{\mathrm{Ref}}}{a} + 1\right)^{1/c} \tag{15}$$

and find $T_{\mathrm{ref}} = 1351$ K, $a = 16.304$ GPa, and $c = 1.8331$. To calculate the shock temperatures along the principal and porous Hugoniots, we use our data along the isentrope as a reference curve and we assume copper behaves as a quasiharmonic Debye solid [44], with $\theta_0 = 343.5$ K. We find that the principal Hugoniot intersects the high-pressure melt curve at 224 GPa, which is in good agreement with the measured critical shock pressure for incipient melting of

232 GPa [38]. This agreement is surprisingly good, given that we did not apply any anharmonic or electronic contributions to the heat capacity. We then assume that copper loses all strength for shock temperatures above the melt curve. These corrected hydrostatic Hugoniot points are used in the calculation of the Grüneisen parameters and the stress along the principal isentrope.

4. Summary of the method for reducing shockless compression data to an isentrope

At this point, all aspects of correcting the shockless compression data to the principal isentrope have been described in Secs. III B 1, III B 2, and III B 3. However, the procedure is slightly complicated as some of the terms in the correction require information about the isentrope. Therefore, we use an iterative procedure to self-consistently solve for the pressure along the isentrope. This iterative procedure is as follows:

(1) Determine a model for the density dependence of the Grüneisen parameter using available Hugoniot data and assuming our shockless compression data represent an isentrope, see Sec. III B 1.

(2) Fit the strength data on the Hugoniot of copper to the Steinberg-Guinan model by scaling Y_0. Model the strength along the ramp compression path based upon the fit to Hugoniot strength data and corrected for the lower temperature along the shockless compression path, see Sec. III B 2.

(3) Calculate the plastic work heating and the thermal pressure from plastic work heating along the shockless compression path using Eqs. (8) and (10).

(4) Determine the pressure along the isentrope by subtracting the deviatoric stress and the thermal pressure from the shockless compression path, Eqs. (7) and (10).

(5) Calculate the plastic work heating at each Hugoniot point below the melt curve using Eq. (13).

(6) Determine the pressure along the hydrostatic Hugoniot states by subtracting the deviatoric stress and thermal pressure, Eq. (14).

(7) Repeat steps 1–6 with the revised model for the isentrope, hydrostatic Hugoniot points, and Grüneisen parameter.

The corrections for the strength, and thermal pressure due to plastic work heating are only a few percent, Fig. 7, and consequently, this procedure converges in only two iterations. To determine the pressure along the 298 K isotherm, one must subtract the thermal pressure from the isentrope at the elevated temperature along the isentrope, T_s,

$$P_{298} = P_s - \gamma\rho[E_{th.}(T_s) - E_{th.}(298))], \qquad (16)$$

where $E_{th.}$ is the thermal energy at density ρ determined from the Debye integral [44] and the temperature along the isentrope is determined from integrating the thermodynamic derivative, $\gamma = \frac{\partial ln T_s}{\partial ln \rho}$.

As in Ref. [4], a higher order Vinet equation of state was then fit to the isentrope, isotherm, and shockless compression paths. The fitting form is

$$P(X) = 3K_0[(1 - X^{1/3})/X^{2/3}]\exp[\eta(1 - X^{1/3}) + \beta(1 - X^{1/3})^2 + \psi(1 - X^{1/3})^3] \qquad (17)$$

where $X = \rho_0/\rho$, and the best fit parameters K_0, η, β, and ψ are described in Table I. The maximum deviation between the fits and the data is 3 GPa at the peak stress state and significantly better at lower pressures; however, the fits are to be used as interpolating functions and are not necessarily valid in extrapolation.

TABLE I. Best fit parameters for the third order Vinet fit, Eq. (17), to the shockless compression data, the principal isentrope, and the 298 K isotherm starting at an initial density of 8.939 g cm^{-3}. For the purposes of error propagation, also shown are fits to the upper and lower 1-σ uncertainty bounds on each fit.

Thermodynamic Path	K_0 [GPa]	η	β	ψ
Shockless Expt.	143.39	6.109	2.1348	4.567
Shockless: Upper	151.52	4.9902	12.858	−23.575
Shockless: Lower	135.4	7.2838	−9.1176	34.055
Principal Isentrope	136.35	7.1173	−7.1245	30.58
Isentrope: Upper	144.01	6.0987	2.5918	5.2783
Isentrope: Lower	128.8	8.1918	−17.365	57.209
298 K Isotherm	127.61	8.151	−14.452	49.034
Isotherm: Upper	134.69	7.1621	−5.0546	24.726
Isotherm: Lower	120.62	9.1941	−24.357	74.617

In Figs. 8 and 9, we present the 298 K isotherm determined from this study. One can see that the isotherm agrees within 2% of that of Ref. [9] up to 65 GPa, where the thermal pressure on the Hugoniot is starting to no longer be negligible. Beyond 65 GPa, our 298 K isotherm is slightly stiffer than the results of Refs. [9] and [4], by about 6 GPa at 150 GPa, which is just outside our 1-σ uncertainty of 5 GPa. It is interesting to see that careful fitting of high-accuracy but low-pressure thermodynamic data on copper by Holzapfel [45], with a smooth extrapolation to the Fermi gas limit yields a nearly perfect agreement with the isotherm determined in this paper.

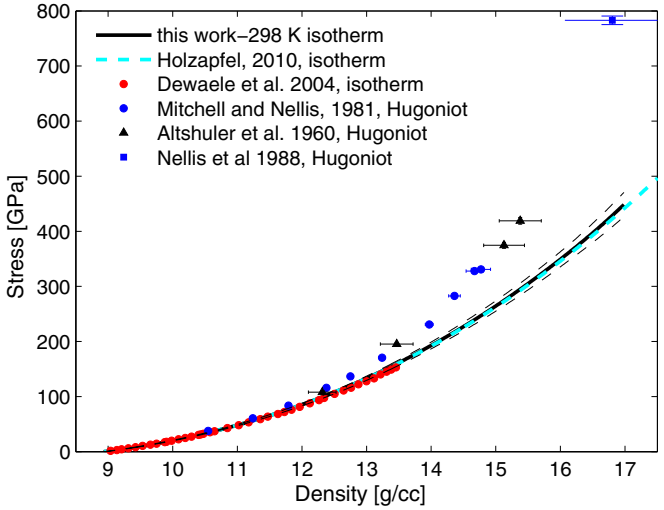

FIG. 8. Equation of state data for copper on the principal Hugoniot and the 298 K isotherm. Shown are Hugoniot data from Mitchell and Nellis [34], Altshuler *et al.* [33], and Nellis *et al.* [35]; and isotherms from Dewaele *et al.* [9], Holzapfel [45], and this paper.

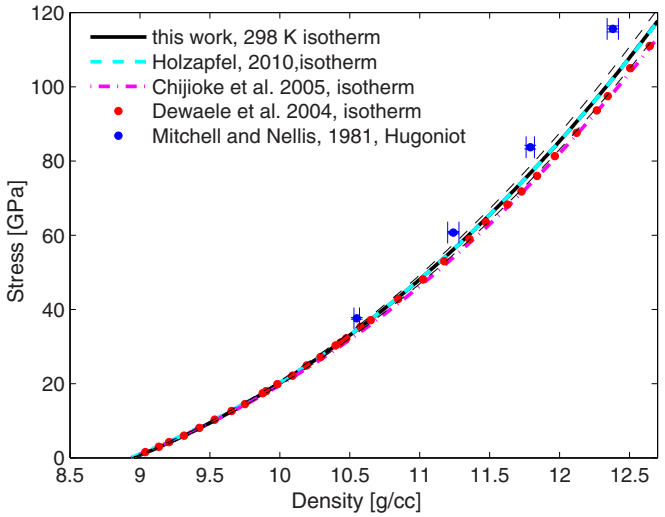

FIG. 9. Equation of state data for copper up to 120 GPa. Shown are Hugoniot data from Mitchell and Nellis [34], and isotherms from Dewaele *et al.* [9], Chijioke *et al.* [4], Holzapfel [45], and this paper.

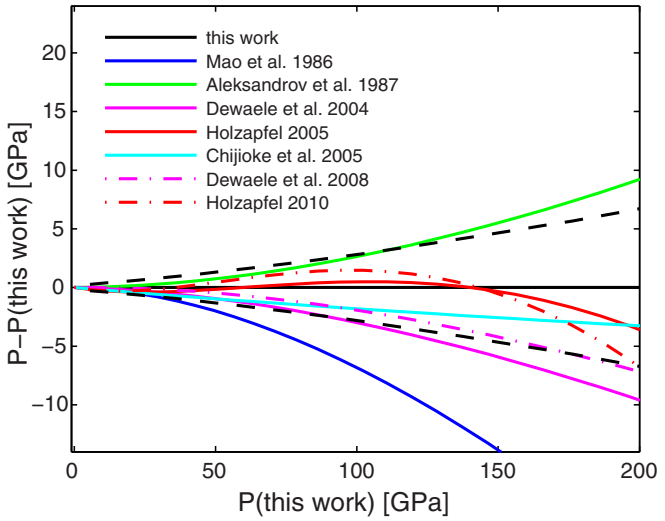

FIG. 10. Comparison of fits to the pressure dependence of the ruby R1 line by Mao *et al.* [46], Aleksandrov *et al.* [49], Dewaele *et al.* [9], Holzapfel [51], Chijioke *et al.* [48], Dewaele *et al.* [52], Holzapfel [45], and this paper. Also shown as black dashed lines are the 1-σ uncertainty bounds on the ruby R1 line calibration of this work. Above 150 GPa, these fits are no longer constrained by data and are presented as extrapolations for comparison purposes.

C. Ruby R1-line calibration

The most common pressure standard within the high pressure diamond anvil cell community is the ruby R-line luminescence [46,47]. Utilizing the quasihydrostatic compression data on copper and ruby presented in Ref. [9], we are able to recalibrate the high-pressure ruby scale using our 298 K isotherm for copper. Here we assume the standard power law expansion for the hydrostatic pressure as a function of the shift in the Ruby R1 line [3],

$$P = \frac{A}{B}\left[\left(\frac{\lambda}{\lambda_0}\right)^B - 1\right] \tag{18}$$

where we find the best fit parameters A = 1915.1 GPa and B = 10.603.

The main source of uncertainty in this ruby calibration is the uncertainty in the copper isotherm, ∼3% in stress at 150 GPa, see Table I for upper and lower bounds. Reference [48] notes the possibility of a 1−2% systematic uncertainty in the stress due to potential nonhydrostatic stresses in the medium used in the diamond anvil cell (DAC) experiments of Ref. [9], which also contributes to the uncertainty in our ruby calibration. Other sources of uncertainty, such as the determination of the R1 line position and the density of copper as determined by XRD in the DAC, are small [9].

In Fig. 10, we present a comparison of our ruby calibration with the ruby calibrations of Mao *et al.* [46], Aleksandrov *et al.* [49], Holzapfel *et al.* [50], Dewaele *et al.* [9], and Chijioke *et al.* [48]. The comparisons are plotted to 200 GPa to show how each of the fits extrapolates, however, the data upon which these fits are based only extend to pressures as high as 150 GPa [9]. One can see that the ruby calibration fits from Refs. [45,48,51] are well within the error bars of this work and that the ruby calibration from Refs. [9,49] are 1-σ away from this revised fit.

IV. DISCUSSION

The dominant contribution to the uncertainty in the isotherm of copper is the random experimental errors associated with the uncertainty in the step thicknesses, the uncertainty in the relative timing of the free-surface velocity profiles, and the uncertainty in the measured free-surface velocity of the shockless compression experiments. These separate uncertainties all contribute relatively equally to the total random experimental uncertainty in stress at a given density, ranging from ∼2% at 50 GPa to ∼4.5% at 450 GPa. The other major sources of uncertainty are the high-pressure strength of copper, ∼1%, the Taylor-Quinney factor, ∼0.3%, and the Grüneisen model, ∼0.2%.

These uncertainty contributions are not, however, unique to shockless compression experiments. For shock experiments below the melt temperature, there will be a deviatoric stress contribution to the longitudinal stress and also thermal pressure generated from plastic work heating. The amount of plastic work that goes into thermal energy, and therefore thermal pressure, is still parameterized by the Taylor-Quinney factor. For shock temperatures above the melt curve, there is significant uncertainty in the latent heat of melting at constant volume.

Where this thermomechanical reduction technique for obtaining isotherms from shockless compression data becomes much more accurate than shock wave reduced isotherms is at pressures well above the bulk modulus, where several tens of percent corrections are required from the pressure at the Hugoniot state to the pressure on the isotherm. As an example, at a density of 17 g cm^{-1}, the pressure on the 298 K isotherm is ∼450 GPa, whereas the pressure on the principal Hugoniot is ∼780 GPa, consequently, a thermal pressure correction of 330 GPa is required for the shock wave data. For an assumed 10−25% uncertainty in the Grüneisen parameter and a 5%

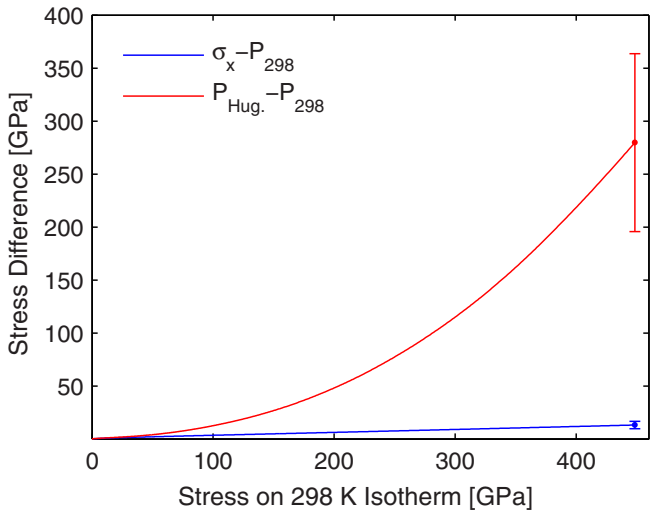

FIG. 11. Sum total of the required corrections and associated uncertainties for reducing shock compression data (red) and shockless compression data (blue) to the 298 K isotherm of copper.

uncertainty in the Hugoniot pressure [34], the total uncertainty in the SWRI would range between 50 and 100 GPa, or two to four times the uncertainty in the isotherm obtained from reducing shockless compression data. A comparison of the required corrections for the SWRI-technique and the technique described here are presented in Fig. 11. The specific crossover pressure where isotherms reduced from shockless compression experiments becomes more accurate than SWRI's depends most sensitively on the uncertainty in the Grüneisen parameter. If one assumes a 10% uncertainty in the Grüneisen parameter, the SWRI will be more accurate up to 250 GPa on the isotherm; however, if one assumes a 25% uncertainty in the Grüneisen parameter then the SWRI will be more accurate only up to ∼70 GPa.

Furthermore, as two-stage diamond anvil cells become more prevalent in the static high-pressure community, the materials used as pressure standards will reach densities where the SWRI technique is no longer viable. Shockless or multishock techniques will be the only means of obtaining accurate pressure calibrations in the terapascal regime.

V. CONCLUSIONS

We have obtained shockless compression data on copper to over 450 GPa using a magnetically applied pressure drive at the Sandia Z Machine. The free-surface velocity data were analyzed using the ILA technique to obtain the Lagrangian sound speed as a function of particle velocity. The Lagrangian sound speed was then integrated to determine an absolute stress-density path. The available data on the high-pressure strength of copper was combined to constrain a modified Steinberg-Guinan strength model. A Mie-Grüneisen Debye thermal model was then iteratively fit to the shockless compression data and the available principal and porous Hugoniot data. The shockless compression stress-density data were corrected for the deviatoric stress and thermal pressure due to plastic work heating to generate a nearly absolute principal isentrope. The principal isentrope was then corrected using our best fit Mie-Grüneisen Debye model to obtain the room temperature isotherm of copper to 450 GPa with an uncertainty of less than 5% at the highest pressures obtained. A high precision fit to the shockless compression data, the isentrope, the isotherm, and a ruby calibration are presented for immediate use for the purposes of pressure calibration within a diamond anvil cell.

ACKNOWLEDGMENTS

The authors wish to acknowledge the support of the large interdisciplinary team it takes to design, fabricate, and execute experiments on the Z machine. We also thank Marius Millot, Tom Arsenlis, and Rip Collins for helpful comments on the paper. This work was performed under the auspices of the U.S. Department of Energy by Lawrence Livermore National Laboratory under Contract No. DE-AC52-07NA27344. Sandia National Laboratories is a multiprogram laboratory managed and operated by Sandia Corporation, a wholly owned subsidiary of Lockheed Martin Corporation, for the U.S. Department of Energy's National Nuclear Security Administration under Contract No. DE-AC04-94AL85000.

[1] J. J. Lissauer and D. J. Stevenson, Formation of giant planets, in *Protostars and Planets V*, edited by B. Reipurth, D. Jewitt, and K. Keil (University of Arizona Press, Phoenix, AZ, 2006), pp. 591–606.

[2] D. M. Trots, A. Kurnosov, T. B. Ballaran, S. Tkachev, K. Zhuravlev, V. Prakapenka, M. Berkowski, and D. J. Frost, The Sm:YAG primary fluorescence pressure scale, J. Geophys. Res.: Solid Earth **118**, 5805 (2013).

[3] H. K. Mao, P. M. Bell, J. W. Shaner, and D. J. Steinberg, Specific volume measurements of Cu, Mo, Pd, and Ag and calibration of the ruby R1 fluorescence pressure gauge from 0.06 to 1 Mbar, J. Appl. Phys. **49**, 3276 (1978).

[4] A. D. Chijioke, W. J. Nellis, and I. F. Silvera, High-pressure equations of state of Al, Cu, Ta, and W, J. Appl. Phys. **98**, 073526 (2005).

[5] S. Tateno, K. Hirose, Y. Oshishi, and Y. Tatsumi, The structure of iron in Earth's inner core, Science **330**, 359 (2010).

[6] L. Dubrovinsky, N. Dubrovinskaia, V. B. Prakapenka, and A. M. Abakumov, Implementation of micro-ball nano diamond anvils for high-pressure studies above 6 Mbar, Nat. Commun. **3**, 1163 (2012).

[7] L. Dubrovinsky, N. Dubrovinskaia, E. Bykova, M. Bykov, V. B. Prakapenka, C. Prescher, K. Glazyrin, H. P. Lierman, M. Hanfland, M. Ekholm, Q. Feng, L. V. Pourovskii, M. I. Katsnelson, J. M. Wills, and I. A. Abrikosov, The most incompressible metal osmium at static pressures above 750 gigapascals, Nature (London) **525**, 226 (2015).

[8] Y. Wang, R. Ahuja, and B. Johansson, Reduction of shock-wave data with mean-field potential approach, J. Appl. Phys. **92**, 6616 (2002).

[9] A. Dewaele, P. Loubeyre, and M. Mezouar, Equations of state of six metals above 94 GPa, Phys. Rev. B **70**, 094112 (2004).

[10] M. E. Savage *et al.*, An overview of pulse compression and power flow in the upgraded Z pulsed power driver, in *2007 IEEE Pulsed Power Conference* (IEEE, 2007), Vol. 1–4, p. 979.
[11] R. W. Lemke, M. D. Knudson, and J.-P. Davis, Magnetically driven hyper-velocity launch capability at the Sandia Z accelerator, Int. J. Impact Engineering **38**, 480 (2011).
[12] R. F. Smith, J. H. Eggert, R. Jeanloz, T. S. Duffy, D. G. Braun, J. R. Patterson, R. E. Rudd, J. Biener, A. E. Lazicki, A. V. Hamza, J. Wang, T. Braun, L. X. Benedict, P. M. Celliers, and G. W. Collins, Ramp compression of diamond to five terapascals, Nature (London) **511**, 330 (2014).
[13] J.-P. Davis, Experimental measurement of the principal isentrope for aluminum 6061-T6 to 240 GPa, J. Appl. Phys. **99**, 103512 (2006).
[14] D. K. Bradley, J. H. Eggert, R. F. Smith, S. T. Prisbrey, D. G. Hicks, D. G. Braun, J. Biener, A. V. Hamza, R. E. Rudd, and G. W. Collins, Diamond at 800 GPa, Phys. Rev. Lett. **102**, 075503 (2009).
[15] J.-P. Davis, J. L. Brown, M. D. Knudson, and R. W. Lemke, Analysis of shockless dynamic compression data on solids to multi-megabar pressures: Application to tantalum, J. Appl. Phys. **116**, 204903 (2014).
[16] J. H. Eggert, R. F. Smith, D. C. Swift, R. E. Rudd, D. E. Fratanduono, D. G. Braun, J. A. Hawreliak, J. M. McNaney, and G. W. Collins, Ramp compression of tantalum to 330 GPa, High Pressure Res. **35**, 339 (2015).
[17] J.-P. Davis, C. Deeney, M. D. Knudson, R. W. Lemke, T. D. Pointon, and D. E. Bliss, Magnetically driven isentropic compression to multimegabar pressures using shaped current pulses on the Z accelerator, Phys. Plasmas **12**, 056310 (2005).
[18] J. B. Aidun and Y. M. Gupta, Analysis of lagrangian gauge measurements of simple and nonsimple plane-waves, J. Appl. Phys. **69**, 6998 (1991).
[19] S. Sheffield, R. Gustavsen, and R. Alcon, In-situ magnetic gauging technique used at LANL-method and shock information obtained, in *Shock Compression of Condensed Matter - 2000*, edited by M. Furnish, L. Chhabildas, and R. Hixson (American Institute of Physics, Melville, NY, 2006), pp. 1207–1210.
[20] J. R. Maw, A characteristics code for analysis of isentropic compression experiments, in *Shock Compression of Condensed Matter - 2003*, edited by M. Furnish, Y. Gupta, and J. Forbes (American Institute of Physics, Melville, NY, 2004), Vol. 706, pp. 1217–1220.
[21] S. D. Rothman and J. Maw, Characteristics analysis of isentropic compression experiments, J. Phys. IV (France) **134**, 745 (2006).
[22] D. E. Fratanduono, R. F. Smith, D. G. Braun, J. R. Patterson, R. G. Kraus, T. S. Perry, A. Arsenlis, G. W. Collins, and J. H. Eggert, The effect of nearly steady shock waves in ramp compression experiments, J. Appl. Phys. **117**, 245903 (2015).
[23] D. L. Preston, D. L. Tonks, and D. C. Wallace, Model of plastic deformation for extreme loading conditions, J. Appl. Phys. **93**, 211 (2003).
[24] G. Bazan, ASCI code calculations of supernova hydrodynamic instabilities, in *Proceedings from the 2nd International Workshop on Laboratory Astrophysics with Intense Lasers, Livermore, CA, 1998*, edited by B. A. Remington (SciTech Connect, Washington, DC, 1998), UCRL-ID-131978.
[25] J. H. Carpenter (private communication).
[26] D. J. Steinberg, S. G. Cochran, and M. W. Guinan, A constitutive model for metals applicable at high-strain rate, J. Appl. Phys. **51**, 1498 (1980).
[27] R. von Mises, Mechanik der festen korper im plastisch deformablen zustand, Nachr. Ges. Wiss. Gottingen **1**, 582 (1913).
[28] G.-R. Fowles, Shock wave compression of hardened and annealed 2024 aluminum, J. Appl. Phys. **32**, 1475 (1961).
[29] G. I. Taylor and H. Quinney, The latent energy remaining in a metal after cold working, Proc. R. Soc. London **143**, 307 (1934).
[30] D. Rittel, A. A. Kidane, M. Alkhader, A. Venkert, P. Landau, and G. Ravichandran, On the dynamically stored energy of cold work in pure single crystal and polycrystalline copper, Acta Mater. **60**, 3719 (2012).
[31] R.-R. Boade, Compression of porous copper by shock waves, J. Appl. Phys. **39**, 5693 (1968).
[32] S. P. Marsh, *LASL Shock Hugoniot Data* (University of California Press, Berkeley, California, 1980).
[33] L. Al'tshuler, S. B. Kormer, A. A. Bakanova, and R. F. Trunin, Equation of state for aluminum, copper, and lead in the high pressure region, Sov. Phys. JETP **11**, 573 (1960).
[34] A. C. Mitchell and W. J. Nellis, Shock compression of aluminum, copper, and tantalum, J. Appl. Phys. **52**, 3363 (1981).
[35] W. J. Nellis, J. A. Moriarty, A. C. Mitchell, M. Ross, R. G. Dandrea, N. W. Ashcroft, N. C. Holmes, and G. R. Gathers, Metals Physics at Ultrahigh Pressures: Aluminum, Copper, and Lead as Prototypes, Phys. Rev. Lett. **60**, 1414 (1988).
[36] Y. B. Zel'dovich and Y. P. Raizer, *Physics of Shock Waves and High-Temperature Hydrodynamic Phenomena* (Dover Publications, Mineola, New York, 1966).
[37] W. B. Holzapfel, M. Hartwig, and W. Sievers, Equations of state for Cu, Ag, and Au for wide ranges in temperature and pressure up to 500 GPa and above, J. Phys. Chem. Ref. Data **30**, 515 (2001).
[38] D. Hayes, R. S. Hixson, and R. G. McQueen, High pressure elastic properties, solid-liquid phase boundary and liquid equation of state from release wave measurements in shock-loaded copper, in *Shock Compression of Condensed Matter - 1999*, edited by M. Furnish, L. C. Chhabildas, and R. S. Hixson (American Institute of Physics, Melville, NY, 2000), p. 483.
[39] L. D. Chhabildas and J. R. Asay, Time-resolved wave profile measurements in copper to megabar pressures, in *Proceedings of Eighth AIRAPT and 19th EHPRG*, edited by T. Johanisson, C. M. Backman, and L. Tegner (Institute of Physical Chemistry, University of Uppsala, Uppsala, Sweden, 1981), pp. 183–189.
[40] L. Al'tshuler, S. B. Kormer, A. A. Bakanova, and R. F. Trunin, Strength and elasticity of iron and copper at high shock-wave compression pressures, Zh. Prikl. Mekh. Tekh. Fiz. **6**, 159 (1971).
[41] E. M. Bringa, K. Rosolankova, R. E. Rudd, B. A. Remington, J. S. Wark, M. Duchaineau, D. H. Kalantar, J. Hawreliak, and J. Belak, Shock deformation of face-centred-cubic metals on sub nanosecond timescales, Nat. Mater. **5**, 805 (2006).
[42] D. C. Swift, A. Seifter, D. B. Holtkamp, V. W. Yuan, D. Bowman, and D. A. Clark, Explanation of anomalous shock temperatures in shock-loaded Mo samples measured using neutron resonance spectroscopy, Phys. Rev. B **77**, 092102 (2008).
[43] Y. N. Wu, L. P. Wang, Y. S. Huang, and D. M. Wang, Melting of copper under high pressures by molecular dynamics simulation, Chem. Phys. Lett. **515**, 217 (2011).

[44] C. Kittel and H. Kroemer, *Thermal Physics* (W. H. Freeman and Company, New York, 1980).

[45] W. B. Holzapfel, Equations of state for Cu, Ag, and Au and problems with shock wave reduced isotherms, High Pressure Res. **30**, 372 (2010).

[46] H. K. Mao, J. Xu, and P. M. Bell, Calibration of the ruby pressure gauge to 800 mbar under quasi-hydrostatic conditions, J. Geophys. Res. **91**, 4673 (1986).

[47] K. Syassen, Ruby under pressure, High Pressure Res. **28**, 75 (2008).

[48] A. D. Chijioke, W. J. Nellis, A. Soldatov, and I. F. Silvera, The ruby pressure standard to 150 GPa, J. Appl. Phys. **98**, 114905 (2005).

[49] I. V. Aleksandrove, A. F. Goncharov, A. N. Zisman, and S. M. Stishov, Diamond at high pressures: Raman scattering of light, equation of state, and high-pressure scale, Sov. Phys. JETP **66**, 384 (1987).

[50] W. B. Holzapfel, Refinement of the ruby luminescence pressure scale, J. Appl. Phys. **93**, 1813 (2003).

[51] W. B. Holzapfel, Progress in the realization of a practical pressure scale for the range 1-300 GPa, High Pressure Res. **25**, 87 (2005).

[52] A. Dewaele, M. Torrent, P. Loubeyre, and M. Mezouar, Compression curves of transition metals in the Mbar range: Experiments and projector augmented-wave calculations, Phys. Rev. B **78**, 104102 (2008).